ISSN: 0976-3031

Available Online at http://www.recentscientific.com

CODEN: IJRSFP (USA)

International Journal of Recent Scientific Research
Vol. 9, Issue, 8(C), pp. 28407-28416, August, 2018

International Journal of Recent Scientific Research

DOI: 10.24327/IJRSR

Research Article

THERMAL EFFECTS ON THE FAILURE MECHANISMS OF HYBRID METAL-COMPOSITE MULTI-BOLTS JOINTS

Calin-Dumitru COMAN*

Department of Structures and Materials, National Institute of Aerospace Research INCAS Bucharest, Romania

DOI: http://dx.doi.org/10.24327/ijrsr.2018.0908.2455

ARTICLE INFO

Article History:

Received 13th May, 2018
Received in revised form 11th June, 2018
Accepted 8th July, 2018
Published online 28th August, 2018

Key Words:

Progressive Damage Analysis, Temperature, Failure Mechanisms.

ABSTRACT

This paper presents the thermal effects on the damage initiation and growth in the CFRP (Carbon Fiber Reinforced Polymer) composite laminated plate of the hybrid metal-composite multi-bolted joints. A detailed 3D finite element model, incorporating all possible nonlinearities as large deformations, in plane nonlinear shear deformations, elastic properties degradation of the composite material and friction-based full contact is developed to anticipate the temperature changing effects on the progressive damage analysis (PDA) at lamina level and failure modes of metal-composite multi-bolted joints. The PDA material model accounts for lamina nonlinear shear deformation, Hashin-type failure criteria and strain-based continuum degradation rules being developed using the UMAT user subroutine in Nastran commercial software. In order to validate the temperature effects on the failure modes of the joint with protruding and countersunk bolts, experiments were conducted using the SHM (Structural Health Monitoring) technique in the temperature controlled chamber. The results showed that the temperature effects on damage initiation and failure modes has to be taken into account in the design process in order to fructify the high specific strength of the composites. Experimental results were quite accurately predicted by the PDA material model, which proved to be computational efficient and can predict failure propagation and damage mechanism in hybrid metal-composite multi-bolted joints.

INTRODUCTION

The aerospace industry became the most common application field for fiber-reinforced polymer matrix composites (PMCs) due to their lightweight properties (Xiao *etal*, 2005). These structural components are often assembled in conjunction with metal parts using mechanically fastened joints resulting in hybrid metal-composite joints which determinate some challenging problems for mechanical engineers. Poor designed hybrid joints is not only a source of failure, but could lead to a reduction in durability and reliability of the whole structure. Up to nowadays, the researchers studied the failure analysis of composite bolted joints using a method that combines continuum damage mechanics (CDM) (Chaboche *et al*, 1988) with finite element analysis (FEA). In the CDM case, the local damage onset appears at a low values of applied load and damage accumulation is developed with increasing load according to damage propagation lows, which makes the method accurate and able to predict various failure modes.

The major disadvantage of the CDM models is the huge amount of test data required for model calibrations. The progressive damage analysis (PDA) in composite materials, which is based on the stress-strain failure criterion, showed that the material orthotropic properties reduction due to damage initiation is essential for the stress field analysis (Chaboche *et al*, 1987, Lessard *et al*, 1995, Hung *et al*, 1996, Kim *et al*, 1998, Camanho *et al*, 199). A lot of PDA models in research field (Okutan *et al*, 2002, Tserpes *et al*, 2002, Olmedo *et al*, 2012, Kapidz˘ic´ *et al*, 2014)incorporated shear nonlinearity, Hashin type failure criterion and constant elastic properties degradation low for orthotropic materials, which makes the method quite easy to implement and computational efficient. Because these properties degradation models used constant factors for elastic properties reduction due to damage growth, the models weren't be able to predict the bearing final failure.

Models containing continuous degradation rules started to appear in the literature (Zerbst, *et al*, 2010, Kolks *et al*, 2014) to improve the numeric algorithm converge and to obtain a smoother loading-displacement curve. One major disadvantage

Corresponding author:* **Calin-Dumitru COMAN
Department of Structures and Materials, National Institute of Aerospace Research INCAS Bucharest, Romania

of these models is that they focused only on a few types of failure mode and not concerning on various joint failure modes. The composite progressive damage behavior is complex nonlinear phenomena and in conjunction with geometric and contact nonlinearities can lead to divergence of the finite element method (FEM) analysis, mostly in implicit numerical algorithms which implies that a lot of effort is paid for obtaining a converged solution toward to ultimate global structure failure.

The composite materials can withstand with increasing temperature up to 3000 ^{0}C, having good properties in high pressure, low thermal expansion coefficient, high thermal conductivity, high thermal shock resistance and low depression (Egan *et al*, 2014). The difficulties arising from composite materials usage on structural failure problems, are that these materials have anisotropic mechanical properties, brittle and low inter-laminar strength (Olmedo *et al*, 2014). Another issue is the damage and composite materials variation with the temperature as it is described in (da Costa Mattos *et al*, 2014, Reis *et al*, 2013, Reis *et al*, 2015). Airplane structures can be exposed to rush environment conditions which can imply the joints strength loss because of environmental ageing and temperature variations, these topics being studied in research community (Jiang *et al*. 2016, Heshmati *et al*, 2017, Kleffel *et al*, 2017, Agarwal *et al*, 2015, Agarwal *et al*, 2013, Heshmati *et al*, 2016).

In this study it is described and developed a progressive damage analysis using an adequate material model for composite plate that can predict the thermal effects on loading structural behavior and failure modes of hybrid metal-composite bolted joints taking into account all the nonlinearities phenomena involved in load transition trough the joint as geometric nonlinearity which imply large deformations, friction based full nonlinear contact and material nonlinearities due to shear deformations of the lamina, Hashin-type failure criterion and strain-based continuous degradation rules implemented using an user subroutine in commercial Nastran SOL 400 solver. A series of experiments were conducted in order to validate the FE model and PDA results involving the influence of temperature on the failure modes of the hybrid-metal composite joints. The experimental and numerical results fit quite accurate for the influence of temperature on the stiffness and failure load of hybrid metal-composite, bolted joints.

Problem Description

Joint geometry

Single-lap joints (SLJ) with protruding and countersunk bolts were manufactured using both metal and composite materials for the adherents, the geometry of the joint model being presented below (Fig.1). The geometry dimensions were chosen in accordance with ASTM D 5961(2007) standard to induce bearing failure. The in plane dimensions of the each plate are the same as follows: 150 mm length and 50 mm width. The thicknesses are different, 4 mm for the metal plate and 2 mm for the laminated plate. Protruding and countersunk head stainless steel bolts with nominal diameter of 5 mm and 4 mm were installed with 0.5 N m torque level applied in dry conditions. The laminated composite plate was manufactured from carbon-epoxy lamina with fiber volume fraction of 32%. The symmetric stacking sequence is represented by $[0^0/90^0]_{3s}$ using 0.33 mm thickness unidirectional lamina, with the elastic properties presented in Table 1. The metal plate was manufactured from aluminum alloy AA 7075T6 (MMPDS, 2010) and the bolts, nuts and washers were from stainless steel A2-70 (MMPDS, 2010), with the elastic properties presented in Table 1 as well. A group of five specimens were prepared for the thermal effects study on the failure mechanisms in the laminated plate.

Joint geometry definition

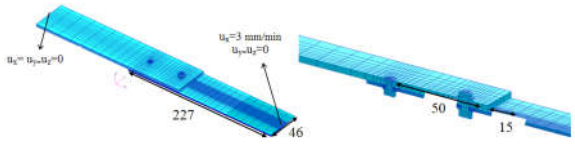

Figure 1 Joint geometry and boundary conditions, all dimensions in mm

Boundary conditions

Regarding the clamping of the joint in the test machine, the boundary conditions imposed on the model are presented (Fig.1). The boundary conditions represent fixing of all three translations on the rectangular axis of the top and bottom surfaces only for the leftmost end of the metal plate and blocking the translations only on Y and Z axis, imposing a prescribed displacement on X axis at the rightmost end of the composite plate. The dimensions of the joint geometry are selected in such way that induce bearing failure in the laminated composite plate (Fig.2).

Bearing failure design

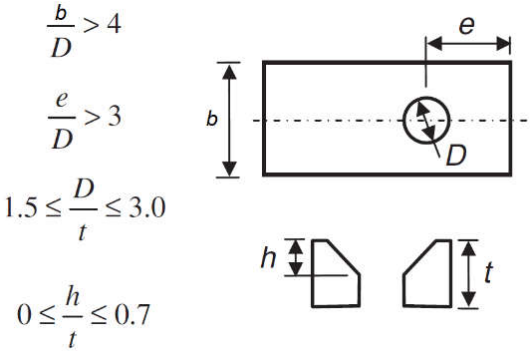

Figure 2 Specimen design for bearing failure mode (Maajid *et al*, 2012)

Material properties

The mechanical properties of all the materials used are presented in Table 1, where the lamina orthotropic directions (1, 2, 3) are the same with global coordinate axis shown in (Fig. 1).The unidirectional elastic properties presented in Table 1 were obtained using ASTM D 3039 (2002), ASTM D 3410 (2007) and ASTM D 5379 (2008) standards on the unidirectional laminated coupons. Regarding the thermal expansion coefficient of the composite plate, it has been used a micro-analysis method to calculate this coefficient at lamina level using the thermal coefficients of the fibers and matrix. The fibers thermal expansion coefficient is α_{fiber}= - 0.41 (10^{-6}/ ^{o}C), (Toray T300 technical data sheet) and, α_{matrix}= 40 (10^{-6}/ ^{o}C) (Derakane Momentum epoxy technical data sheet) for the matrix thermal coefficient. Using these values and equation (1),

the lamina thermal coefficients on the orthotropic axis can be obtained (ECSS-E-HB-32-20, 2011):

$$\alpha_{11}=\frac{E_{fiber}\cdot V_{fiber}\cdot\alpha_{fiber}+E_{matrix}\cdot(1-V_{fiber})\cdot\alpha_{matrix}}{E_{11}}=2\cdot10^{-6}/C \quad (1)$$

$$\alpha_{22}=\alpha_{33}=44\cdot10^{-6}/C \quad (2)$$

Table 1 Material properties

Property	Carbon fiber	Epoxy	Lamina	AA70 75T6	A2-70
Longitudinal modulus E_{11} (MPa)	230000	3200	34433	71016	206000
Transversal modulus E_{22} (MPa)	6000	3200	3610		
Through-thickness modulus, E_{33} (MPa)		3200	3610		
Shear modulus G_{12} (MPa)	18000	1300	2421	26890	75842
Shear modulus G_{23} (MPa)		1300	2421		
Shear modulus G_{13} (MPa)		1300	1561		
Poisson coefficient υ_{12}	0.36	0.35	0.36	0.33	0.36
Poisson coefficient υ_{23}		0.35	0.45		
Poisson coefficient υ_{13}		0.35	0.35		
Longitudinal CTE α (10^{-6}/°C)	-0.4	40	2	24	18
Transversal CTE α (10^{-6}/°C)		40	44		
Through-thickness CTE α (10^{-6}/°C)		40	44		
Longitudinal tensile strength $\sigma_{11,max}^{T}$,(MPa)	3530	86	253	510	800
Longitudinal compression strength $\sigma_{11,max}^{C}$, (MPa)			223	448	400
Transversal compression strength $\sigma_{22,max}^{C}$, (MPa)			74		
In plane shear strength τ_{12}^{max}, (MPa)			30	303	480
Out plane shear strength τ_{23}^{max}, (MPa)			37		
Out plane shear strength τ_{13}^{max}, (MPa)			37		

Experimental setup

After joints installation setup, the specimens were gripped in the 30 kNInstron 3367 universal testing machine connected to a temperature controlled chamber. The used chamber is Instron SFL 3119-400 series, temperature controlled (-70/+250 °C), with liquid CO_2 as frozen agent. The bearing tests were conducted in accordance with ASTM D 5961standard and the specimens were loaded with controlled displacement of 0.3 mm/min until ultimate failure at two temperature values, T=+50°C and T=-50°C.

Experimental setup

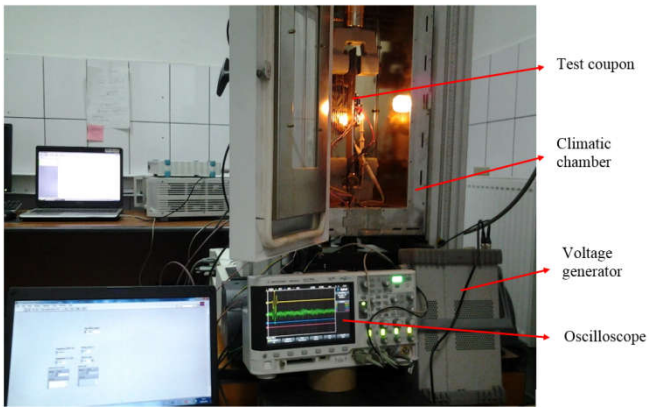

Figure 3 Experimental workbench

Numerical Model Description

A tridimensional finite element model, using linear eight nodes brick elements, was developed in commercial software MSC Patran for the joint model, (Fig. 4). Each separate part was modeled: metal and composite plates, three washers and two combined bolt-nut parts. The plates were meshed with high radial mesh density around each hole, where high strain gradients exists. In order to avoid rigid body motions, light springs were attached to the components not fully constrained, such as the bolts, washers and laminate plate. For simulating the bolt preload due to the torque level, a 330 N axial force was applied in the bolt shank using Bolt Preload Module in Patran.

FE Model

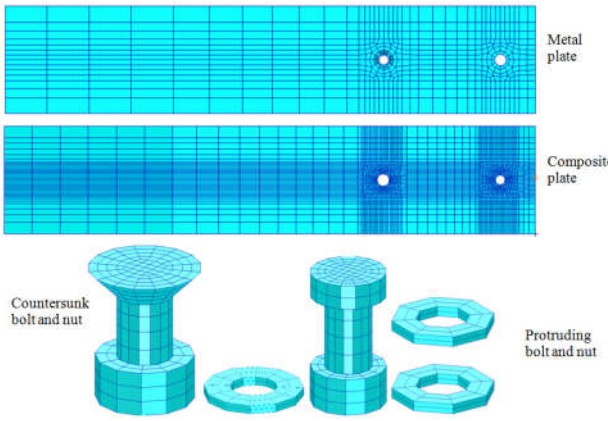

Figure 4 FE components models

The laminated plate is modelled with continuum solid-shell special elements available in MSC Nastran 2012. These special solid elements has bending properties like shells and one integrating point per element. The finite element model has six elements per laminate thickness plate, with one solid-shell element per each ply, thus, stress in each ply can be determined and the correct bending-twisting coupling is obtained. In the 3D model, the contact between the bolts and the holes surfaces is achieved by the direct method of the constraints explained in the following. The method requires the definition of contact bodies, bodies that can be contacted. The bodies in contact may be whole physical bodies (laminated plates, bolt, washer), but it has been shown(McCarthy *et al*, 2005) that it is more efficient to consider sets of elements of these physical bodies in contact, (Fig. 5), because the number of checks for contact between bodies at each iteration of the solution is reduced.

Contact Regions

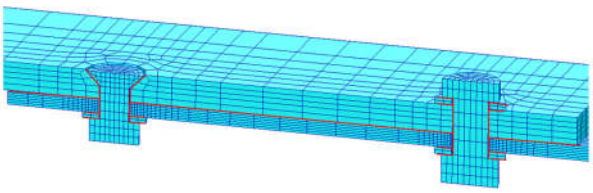

Figure 5 Contact surfaces in 3D FEmodel

The next step in defining nonlinear contact phenomena is the choice between the analytical contact and discreet contact, both of them will be briefly described below. When a node on a part reaches the contact segment on the other part, the node is constraint on this segment along the normal to this segment. In

the case of discrete contact, the linear representation with the finite elements of the contact surface is used for normal detection, which leads to determination of the normal of each element. If the surface is not planar, when the node touching the contact segment on the surface of the other part in contact, being in the tolerated contact area, it is shifted and constrained on the contact segment, making it possible for the moving process and constraint, the surface having a curve, the node is blocking between two differently normal elements due to the discontinuity of the elements normal. This impediment has an adverse effect on the quality of the results as observed by (McCarthy *et al,* 2005) in their work on single bolt joint, single shear of composite materials.

In the case of analytical contact, a smooth Coons surface is constructed through the nodes of the solid contact segment, and then this analytical surface is used to calculate the continuous normal at the contact surface between the two parts, thus solving the problem of node blocking due to the discontinuity of normal of the surface between the parts. This method leads to a better representation of the geometry of the joint, especially its deformation and the accuracy of the numerical results is far superior to the technique of discrete contact (McCarthy *et al,* 2005).

Temperature Effects on Joint Stiffness

Joint stiffness

The effects of the temperature on the joint axial stiffness are presented in this paragraph. The experiment setup is shown in Table 3 for two-bolts, single-lap, metal-composite joints. From the experimental results it was observed that the load-displacement curves are approximately linear between0.2 - 4kN applied loads in the experiment and 0.1-3.8kN in the simulation for temperature T = +50 ^{0}C, but between 0.1-6kN in the experiment and 0.1-8.5 kN in the simulation for temperature T = - 50 ^{0}C, so the stiffness of the joint is determined for these load intervals. The joint load was obtained directly from testing machine, and the displacement was measured with optical extensometers. The load-displacement curves for the two temperature values are presented below (Fig. 8).

Table 2 Experiment setup

Test number	Number of specimens	Torque level (Nm)	Temperature (^{0}C)
1	5	0.5	-50
2	5	0.5	+50

Load-displacement curves

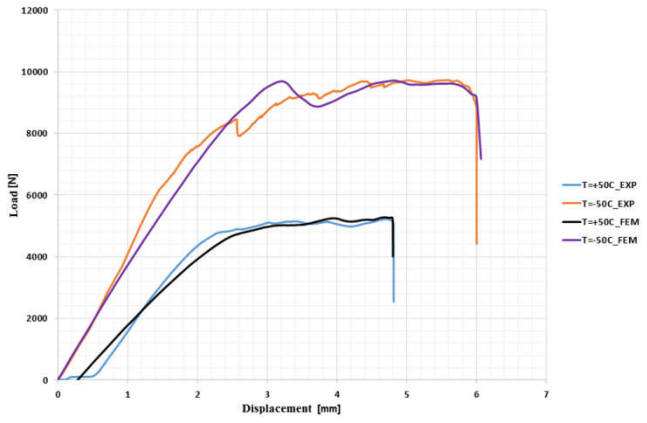

Figure 6 Thermal effects on the load-displacement curves

The first nonlinear segment on the experimental curvefrom (Fig. 6) for temperature T= +50 ^{0}C is explained by the friction between the plates. For low level of the applied load, the forces are transmitted through the friction and the plates don't move relatively, so the shank of the bolt don't bear the hole surface due to the initial clearance in the joint. The joint under investigation has a close tolerance clearance equal to 48 μm for both the holes in the joint, according to f7H10 standard fit tolerances. As long as F > μP, where F is the applied joint load, μ=0.235 is the frictional coefficient between aluminum AA 7075 and CFRP plates as Schon (Schon *et al*, 2004) measured experimentally and P = 330 N is the plates clamping force due to preload, the friction is overcomes and the bolt shank bears the hole surface. From now on, the joint is elastically deformed, the axial stiffness is fully developed and can be determined. The experimental and numerical axial stiffness, calculated as the slope of the approximately linear portions of the load-displacement curves, are presented in Table 3.From Table 3 and (Fig.6), it can be observed that the temperature reduces the stiffness of the hybrid metal-composite joint both in the experiment and simulation results, due to the fact that the matrix became plasticized under high temperature and due to low volume ratio of carbon within the composite material (32 %). As can be seen, the FE model joint is less stiffen than the experimental one which imply that the mesh size was properly chosen.

Table 3 Thermal effects on axial stiffness

Stiffness (kN/mm)		Temperature (^{0}C)
Experiment	Simulation	
4.546	3.971	-50
2.956	2.542	+50

Temperature Effects on Failure Mechanism

Nonlinear shear deformation

In order to take into account the nonlinear behavior of the composite plate within the hybrid metal-composite joint, the simulation must take into account the two most important nonlinear mechanisms: lamina nonlinear shear deformations and stiffness reduction due to damage accumulation at lamina level. These two nonlinearities are taken into account using an external user-defined subroutine named USER_MAT, edited in FORTAN language. USER_MAT calls the modified predefined Nastran user-defined subroutine UMAT, in order to implement the material nonlinearities specified above.

Hahn and Tsai (Hahn and Tsai, 1973) developed the in plane nonlinear shear lamina constitutive model using high order elasticity theory:

$$\gamma_{12} = \frac{\tau_{12}}{G_{12}} + \beta \cdot \tau_{12}^3 \qquad (3)$$

Where β is a material parameter that can be determined by experiments only. Below (Fig. 7), it is shown the experimental curve of the shear deformation γ_{12} as a function of the shear stress τ_{12} obtained using off-axis tension tests on unidirectional laminates. This constitutive relation can be implemented in USER_MAT user subroutine (Ao *et al*, 2016):

$$\tau_{12}^{(t+\Delta t)} = \frac{1+2\cdot\beta\cdot(\tau_{12}^t)^3\cdot(\gamma_{12}^t)^{-1}}{1+3\cdot\beta\cdot G_{12}{}^0\cdot(\tau_{12}^{(t)})^2}\cdot G_{12}{}^0\cdot\gamma_{12}^{t+\Delta t} \qquad (4)$$

Nonlinear shear stress-strain

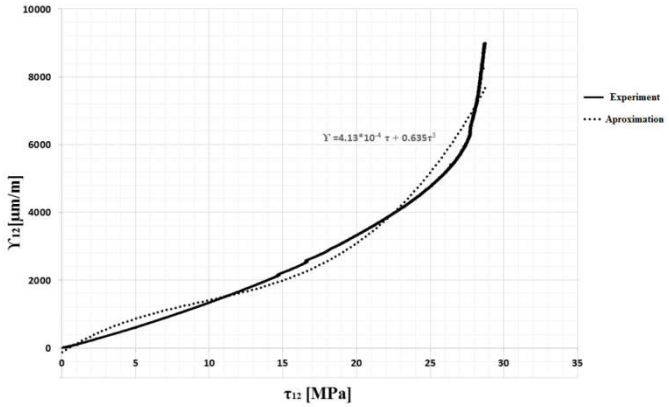

Figure 7 Nonlinear shear stress–strain experimental curve

From the figure above (Fig. 9), by polynomial interpolation, it was obtained the coefficient $\beta = 0.635$ MPa^{-3} for this type of lamina used in the study. The orthotropic stress-strain constitutive relationship is given by equations (5) and (6), (Ao *et al*, 2016):

$$\begin{bmatrix}\sigma_{11}^{t+\Delta t}\\ \sigma_{22}^{t+\Delta t}\\ \sigma_{33}^{t+\Delta t}\end{bmatrix}=\begin{bmatrix}E_{11}B(1-\vartheta_{23}\vartheta_{32}) & E_{22}B(\vartheta_{12}-\vartheta_{13}\vartheta_{32}) & E_{33}B(\vartheta_{13}-\vartheta_{12}\vartheta_{23})\\ E_{22}B(\vartheta_{12}-\vartheta_{13}\vartheta_{32}) & E_{22}B(1-\vartheta_{13}\vartheta_{31}) & E_{22}B(\vartheta_{32}-\vartheta_{12}\vartheta_{31})\\ E_{33}B(\vartheta_{13}-\vartheta_{12}\vartheta_{23}) & E_{22}B(\vartheta_{32}-\vartheta_{12}\vartheta_{31}) & E_{33}B(1-\vartheta_{12}\vartheta_{21})\end{bmatrix}\times\begin{bmatrix}\varepsilon_{11}^{t+\Delta t}\\ \varepsilon_{22}^{t+\Delta t}\\ \varepsilon_{33}^{t+\Delta t}\end{bmatrix} \quad (5)$$

$$\begin{bmatrix}\tau_{12}^{t+\Delta t}\\ \tau_{23}^{t+\Delta t}\\ \tau_{31}^{t+\Delta t}\end{bmatrix}=\begin{bmatrix}\text{Rel.(8)} & 0 & 0\\ 0 & G_{23} & 0\\ 0 & 0 & G_{31}\end{bmatrix}\times\begin{bmatrix}\gamma_{12}^{t+\Delta t}\\ \gamma_{23}^{t+\Delta t}\\ \gamma_{31}^{t+\Delta t}\end{bmatrix} \quad (6)$$

where:

$$B=\frac{1}{1-\vartheta_{12}\vartheta_{21}-\vartheta_{23}\vartheta_{32}-\vartheta_{13}\vartheta_{31}-2\cdot\vartheta_{21}\vartheta_{32}\vartheta_{13}} \quad (7)$$

$$\tau_{12}^{t+\Delta t}=\begin{cases}\frac{1+2\cdot\beta\cdot(\tau_{12}^{t})^{3}\cdot(\gamma_{12}^{t})^{-1}}{1+3\cdot\beta\cdot {G_{12}}^{0}\cdot(\tau_{12}^{t})^{2}}\cdot {G_{12}}^{0}\cdot\gamma_{12}^{(t+\Delta t)}, & FI=0\\ {G_{12}}^{t+\Delta t}\cdot\gamma_{12}^{t+\Delta t}, & FI\geq 1 \text{ and } {G_{12}}^{t+\Delta t}\cdot\gamma_{12}^{t+\Delta t}<\tau_{12}^{init}\\ \tau_{12}^{init}, & FI\geq 1 \text{ and } {G_{12}}^{t+\Delta t}\cdot\gamma_{12}^{t+\Delta t}\geq\tau_{12}^{init}\end{cases} \quad (8)$$

$$FI=max\,(FI_1, FI_2) \quad (9)$$

In relation (8), ${G_{12}}^{0}$ is the initial in-plane shear modulus which is reduced according to degradation rules specified in relation (13), once fiber compression-shear failure happened, FI_1 and FI_2 are defined with relations (10), (11) . The shear stress τ_{12}^{init} is a threshold used to avoid any over-estimation of the shear stress after any failure that can reduce the shear modulus G_{12}.

Failure criteria and continuous degradation rules

The most dominant micro-failure modes for bearing joints are matrix compression, fiber compression and fiber-matrix shear modes, so a grate attention is given for them in this study regarding joint failure mechanisms. For the PDA (Progressive Damage Analysis) of the laminated plate, Hashin (Hashin, 1980) failure criteria for unidirectional tape laminate is used as the failure indexes are calculated with relation (10) for matrix compression and relation(11) for fibers compression-shear:

$$FI_1=\left[\left(\frac{\sigma_{22,\,max}^{C}}{2\cdot\tau_{23}^{max}}\right)^2-1\right]\cdot\frac{\sigma_2+\sigma_3}{\sigma_{22,\,max}^{C}}+\frac{(\sigma_2+\sigma_3)^2}{4\cdot(\tau_{23}^{max})^2}-\frac{\sigma_2\cdot\sigma_3}{(\tau_{23}^{max})^2}+\left(\frac{\tau_{12}}{\tau_{12}^{max}}\right)^2+\left(\frac{\tau_{13}}{\tau_{13}^{max}}\right)^2+\left(\frac{\tau_{23}}{\tau_{23}^{max}}\right)^2+\left(\frac{\sigma_1}{\sigma_{11,\,\max}^{T}}\right)^2 \quad (10)$$

$$FI_2=\left(\frac{\sigma_1}{\sigma_{11.\,max}^{C}}\right)^2+\left(\frac{\tau_{12}}{\tau_{12}^{max}}\right)^2+\left(\frac{\tau_{13}}{\tau_{13}^{max}}\right)^2 \quad (11)$$

Continuous degradation rules for elastic moduli

A strain based degradation rule is proposed for reduction of E_{ii} (i=1..3) as described in the literature (Zhou *et al*, 2014, O'Higgins *et al*, 2007). The fiber or matrix failure initiate at a user-defined failure strain ε_{ii}^{init} and PDA stiffness reductions are performed using relation (12):

$$E_{ii}^{t+\Delta t}=\begin{cases}E_{ii}^{0}\cdot\left(1-d_i\cdot\frac{\varepsilon_{ii}^{t+\Delta t}-\varepsilon_{ii}^{init}}{\Delta\varepsilon_{ii}}\right), & \varepsilon_{ii}^{init}\leq\varepsilon_{ii}^{t+\Delta t}<\varepsilon_{ii}^{init}+\Delta\varepsilon_{ii}\\ E_{ii}^{0}\cdot(1-d_i)\frac{\varepsilon_{ii}^{init}+\Delta\varepsilon_{ii}}{\varepsilon_{ii}^{t+\Delta t}}, & \varepsilon_{ii}^{t+\Delta t}\geq\varepsilon_{ii}^{init}+\Delta\varepsilon_{ii}\end{cases} \quad (12)$$

Where E_{ii}^{0} is the initial modulus of elasticity of lamina on-axis system, presented in Table 1, $\Delta\varepsilon_{ii}$ is a strain step, user-defined parameter to ensure a smooth reduction of the properties upon failure and d_i is the reduction factor. Initial failure strain and corresponding stress ε_{ii}^{init}, σ_{ii}^{init} are determined by simulation for FI=1 according to relation (9).

Continuous degradation rules for shear modulus

On post failure analysis, the in-plane shear modulus G_{12} is reduced using the shear strain $\gamma_{ij}^{t+\Delta t}$ for FI>1, (Zhou *et al*, 2014) and for generalization, we have:

$$G_{ij}=G_{ij}^{0}\left(0.1+0.9\cdot\frac{\gamma_{ij}^{init}}{\gamma_{ij}^{t+\Delta t}}\right),\ i\neq j=1..3 \quad (13)$$

The reduction parameters for E_{ii} (i=1..3) are presented in Table 4 obtained after several parameter tuning iterations.

Table 4 Degradation parameters for elastic moduli

Failure mode	d_i	$\Delta\varepsilon_{ii}$
Fiber shear-compression (i=1)	0.4 5	0.01
Matrix compression (i=2,3)	0.5 7	0.01

Poisson's coefficient reduction

The reduction of the Poisson's ratio is proposed in order to comply with elastic stability of the orthotropic materials, (O'Higgins *et al*, 2007):

$$\vartheta_{12}=\vartheta_{12}^{0}\cdot\sqrt{\frac{E_1E_2^{0}}{E_2E_1^{0}}},\ \vartheta_{13}=\vartheta_{13}^{0}\cdot\sqrt{\frac{E_1E_3^{0}}{E_3E_1^{0}}},\ \vartheta_{23}=\vartheta_{23}^{0}\cdot\sqrt{\frac{E_2E_3^{0}}{E_3E_2^{0}}} \quad (14)$$

SHM method description

A common and useful method for structure health monitoring (SHM) is using the guided waves. The major advantage of these waves is the low energy losing while passing through the structure, which denotes an excellent energy transfer through entire structure. The pioneer of this method is Horace Lamb which published his result for the first time in 1917(Lamb *et al*, 1917). There are two types of propagation modes for these waves: symmetric mode (S_0, S_1…S_n) and anti-symmetric (A_0, A_1…A_n) (Giurgiutiu*et al*, 2002). In usual applications, the most used mode for SHM testing method is the fundamental mode S_0, which has maximum amplitude at high frequency 150-300 Hz and A_0 which has maximum amplitude at low frequency, 30-100 Hz (Giurgiutiu*et al*, 2003). The reason for choosing these two fundamental modes is that they are easier to identify from the oscillation group of modes than the other superior

ones. The SHM testing technique was used to experimentally observe the first ply failure in the laminate plate of the bolted joint. The PWAS devices used in this experiment are produced by STEMiNC company, with the part number SMPL7W7T02412. They have a circular shape with 5 mm diameter and are presented in Fig. 9. The company code of the PWAS piezo-electric material is SM412 and the electro-mechanical properties are presented in the Table 5, (http://www.steminc.com). The input signal is a sinusoidal tone burst type signal having 20V peak to peak amplitude with Hanning window amplitude modulation. This signal includes 3 periods and is generated by an Agilent 33120 signal generator (Fig. 9).

PWAS positions

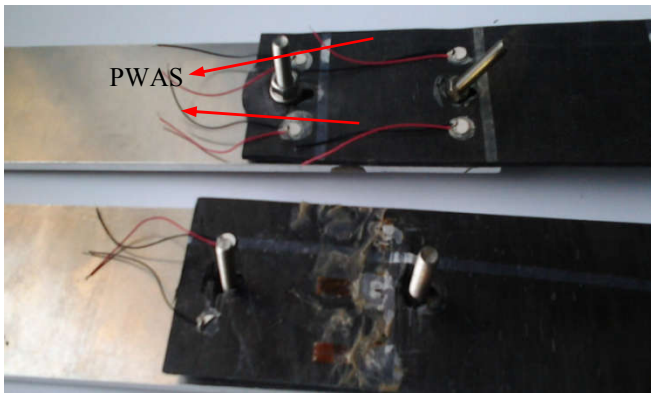

Figure 8 PWAS positions on composite plate

Table 5 Electro-mechanical characteristics of the SM412 material

Property	Symbol	Value	Measurement unit
Electromechanical coupling coefficient	K_p	0.63	
	K_t	0.42	
	K_{31}	0.35	
Frequency constant	N_p	2080	Hz ● m
	N_t	2080	
	N_{31}	1560	
Piezoelectric constant	d_{33}	450	$\times 10^{-12}$m/v
	d_{31}	-190	
	g_{33}	25.6	$\times 10^{-3}$Vm/N
	g_{31}	-12.6	
Elastic Constant	Y_{33}	5.6	$\times 10^{10}$N/m^2
	Y_{11}	7.6	
Mechanical Quality Factor	Q_m	100	
Dielectric Constant	$_{\varepsilon}T_{33/\varepsilon\,0}$	1850	@1KHz
Dissipation Factor	tan δ	1.2	%@1KHz
Curie Temperature	T_c	320	°C
Density	r	7.8	g/cm^3

Wave genetarator and input singnal

a

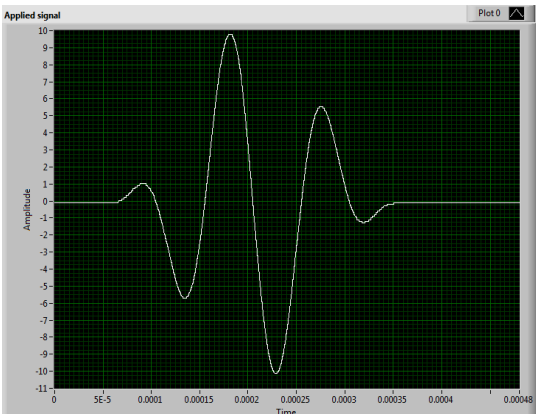

b

Figure 9 Hewlett Packard 33120A arbitrary waveform generator (a) and the input signal (b)

This type of input signal provides a gradual excitation with progressive amplitudes of the joint structure. The received signal is registered by connecting an oscilloscope probe on receiving PWAS. For viewing the input signal also, an oscilloscope probe is connected to the emitting PWAS. This signal is used as reference signal for data processing. All these probes are connected to an Agilent DSO-X 3034A digital storage oscilloscope (Fig.10), which performs the data acquisition.The entire process of data acquisition including the controll of the arbitrary wave form generator and the digital storage oscilloscope is performed by a Labview code running on a PC. This PC is connected using USB and RS232C ports to the other devices (Fig.11).

Ocilloscope

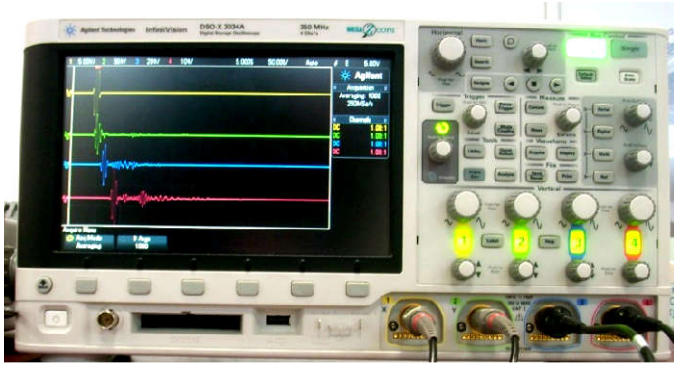

Figure 10 Agilent DSO-X 3034A digital storage oscilloscope

Acquisition diagram

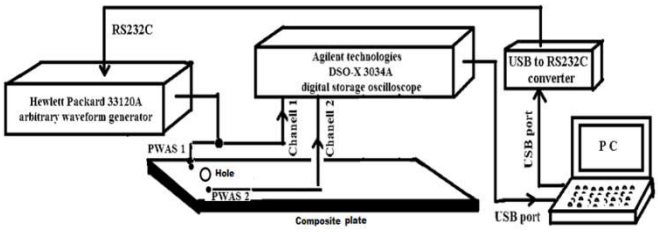

Figure 11 The data acquisition system diagram

RESULTS AND DISCUSIONS

Below (Fig. 12), it is presented the damage initiation effect on the amplitude of the received signal and force-displacement characteristic curve, in order to be able to identify the first ply failure of the laminated plate of the joint. The amplitude curves represent the maximum (peak to peak) amplitudes of each

receiving signals during the test. During a test, the input and output signals of the two PWAS's from the laminated plate are acquisitioned with a period of 2 seconds. It can be clearly seen (Fig. 12) that the amplitude of output signal is increasing with the joint stiffening up to the first lamina failure event. Afterwards the amplitude is decreasing due to the elastic properties degradation in the laminate due to the post failure stage. As a conclusion, it can be considered that SHM method accurately predict the first lamina failure and joint limit load which represents the fiber compression damage at the lamina level, because this local damage corresponds to a significant decreasing of the joint stiffness.

The comparison between experimental and numerical results in terms of the thermal effects on damage initiation and progressive failure mechanism are presented in the following. Load-displacement curves for each temperature value are presented below (Figs. 13 and 14). From (Figs. 13 and 14), it can be seen that the temperature has increased the limit (damage initiation) and ultimate (maximum) loads significantly. At point A on the characteristic load-displacement curves, the fiber and matrix compression damage onset around the hole is evident accordingly to (Fig. 15). At the beginning of the test, the structural response of the joint is dominated by friction between the plates up to 0.5 mm displacement, for T = +50 ^{o} C and 0.05 mm displacement, for T = -50 ^{o} C. From the end of the friction stage up to point A, the structural behavior of the hybrid joint is almost linear with small fluctuations which represents small matrix compression damages, but this do not affect the overall joint stiffness.

Point A represents the first damage initiation point, denoting the limit load of the joint and is located at the major deviation of the force-displacements curves from linear behavior. At this point, the compression fibers damage is onset as an indicator of the bearing failure initiation, despite the fact that the appearance of the fiber-matrix shear damage which is observed in Point A, also. Matrix compression damage is also present at point A, but this does not contribute a lot to the joint stiffness lose, as already mentioned, because fibers have the most important role in joint stiffening, but not the matrix. As can be seen from (Figs. 15) (T=+50 ^{o}C) and 19 (T=-50 ^{o}C), in 0^{o} plies the amount of fibers damage is less than matrix damage, while in 90^{o} plies the two micro level damages have almost the same amount. In (Figs. 15-21), the dark blue color represents the undamaged elements, while the red color states for E^{0}_{ii} (1-d_i) residual stiffness of the elements.

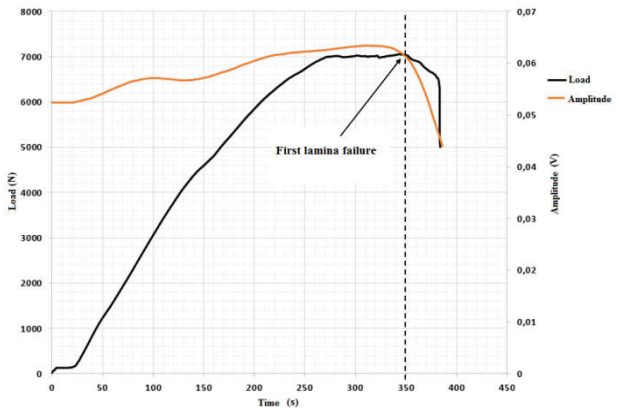

Figure 12 Damage effects on output signal, T= +50 ^{o}C

Characteristic load-displacement curves

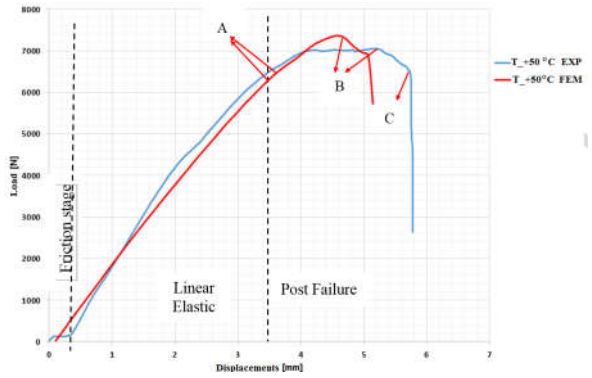

Figure 13 Load-displacement curves, T=+50 ^{o}C

Characteristic load-displacement curves

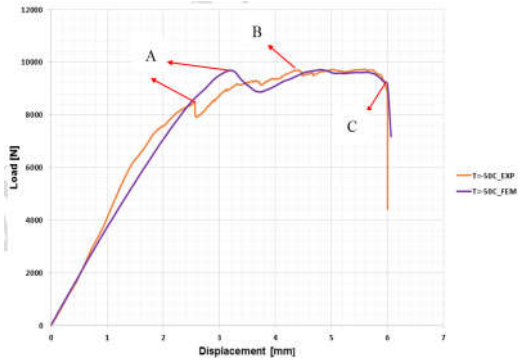

Figure 14 Load-displacement curves, T = -50 ^{o}C

From Fig. 14, it can be observed that the friction static force between the aluminum and composite plates is approximately F_f= 150 N and taking into account the plates clamping force P = 330 N, implies that the real friction coefficient should be equal to:

$$\mu=\frac{F_f}{2\cdot P}=\frac{150}{2\cdot 330}=0.227 \quad (15)$$

This value is quite closer to the values used in numerical simulation μ=0.235, according to Schon [36], which implies that the simulation took into account the friction base phenomena with sufficient accurate. The little difference between the friction coefficient values is due to the fact that in the experiments of this study the surfaces of the two plates were not properly cleaned with ultrasonic technique as Schon did in his work.

In above figures (Figs. 13 and 14), point B represents the joint ultimate failure. After the point A, increasing the applied load, the damage accumulation determines joint stiffness reduction gradually and the characteristic curve becomes nonlinear. From point A up to point B, the post failure stage is completely developed, where the residual stiffness is continuously reduced. On this stage, the fibers compression, matrix compression and fiber-matrix shear damages are increasing on the bearing plane through the whole thickness of the laminate plate, as can be seen from (Figs. 16 and 19). Point C represents the catastrophic final failure of the joint, when fibers compression, matrix compression and fiber-matrix shear damages are extended to a large portion of the laminate plate on the bearing plane, as can be easily seen from (Figs. 17 and 20). The thermal effects on the final failure modes for the two temperatures in this study

can be easily seen from (Fig.17 and 20), where it is observed that for positive temperature (T=+50 ^{0}C) the bearing mode and shear-out is predominant at protruding head bolt hole, while for negative temperature value, the failure mode is bearing for the both holes.

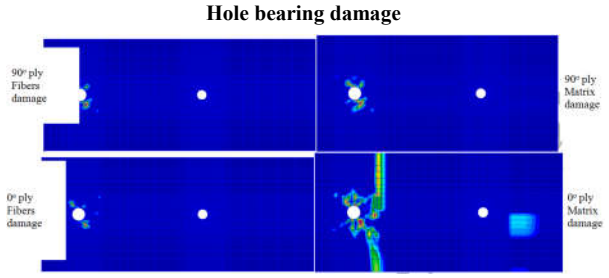

Figure 15 Hole bearing damage onset, point A, T= + 50 ^{o}C

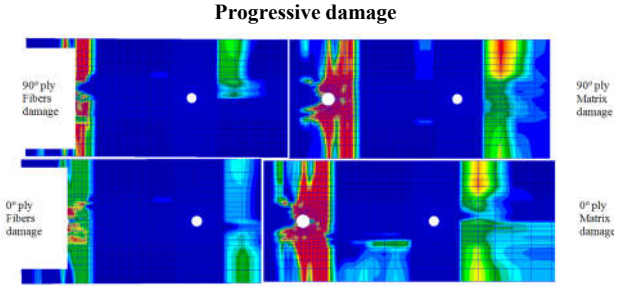

Figure 16 Progressive hole damage, point B, T= + 50 ^{o}C

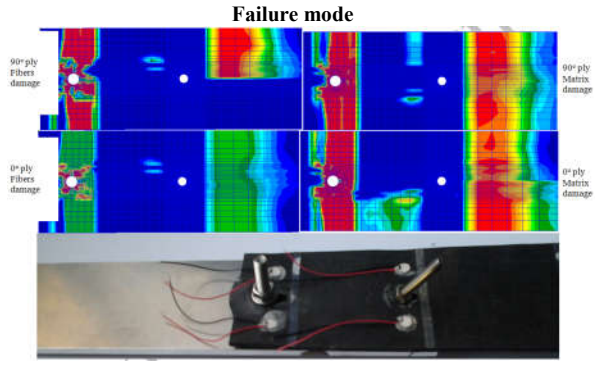

Figure 17 Catastrophic failure, point C, T= + 50 ^{o}C

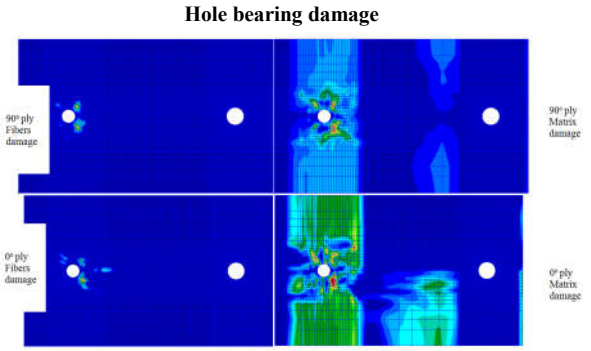

Figure 18 Hole bearing damage, point A, T= - 50 ^{o}C

A summary of the thermal effects on the final failure modes of protruding and countersunk multi-bolts hybrid metal-composite joint is presented in Table 6 and (Figs. 21) in terms of limit load (L.L) and ultimate load joint capacity. From Table 6 it can be seen that, the temperature increase reduces the limit and ultimate loads, thus reduces the hybrid metal-composite joint strength.

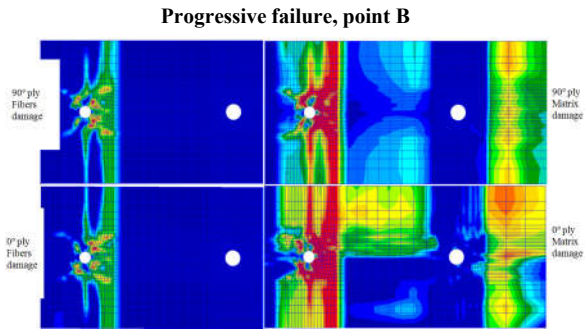

Figure 19 Progressive hole damage, point B, T= - 50 ^{o}C

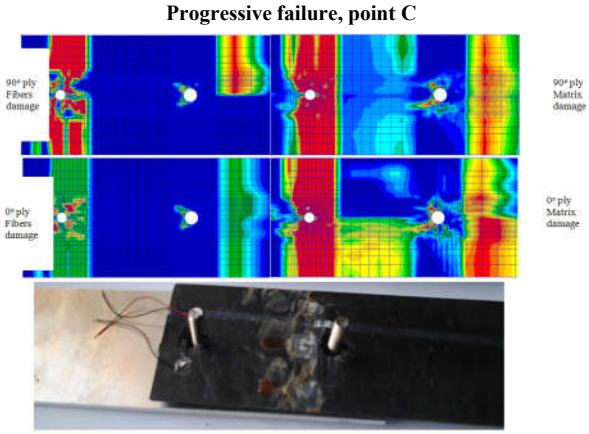

Figure20 Catastrophic failure, point C, T= - 50 ^{o}C

The final mode of failure is changing with the temperature as can be clearly seen from Table 7, for T = -50 ^{0}C the final joint failure mode is bearing while for T = +50 ^{0}C, this is bearing and shear-outmixt mode. It can be observed from Table 6 that negative values of temperature can confer a higher strength of the structure due to the fact that the composite material becomes much stiffen at low temperature. Keeping in mind that the most airplanes operate at high altitude and low temperature, the temperature effects on the joint strength are beneficial, while the preferred mode of failure is bearing due to the ductile mode of failure.

So, the temperature is a very important parameter in the design process of reliable joint and has to be taken into account very carefully due to the different thermal coefficients of expansion of the materials and different modes of final failure at positive and negative values of temperature for hybrid metal-composite joints. In generally, the joints are designed to fail in ductile bearing mode for the benefits of the stress relief in the hole vicinity. The positive value of temperature has its own benefits, underlying that for + 50 ^{o}C it was observed in the experiments the yielding process before the final failure due to the low fiber volume ratio (32 %) in laminate's layers and this yielding contributes to the stress relief.

Table 6 Thermal effects on final failure mode of the joint

Torque [Nm]	Temperature [^{o}C]	F_{LL}[N]		F_{UL} [N]		Failure mode
		EXP	FEM	EXP	FEM	
0.5	+50	6200	6300	7050	7400	Bearing+shear-out
0.5	-50	8400	9800	9830	9815	Bearing

Thermal influence on joint load capacity

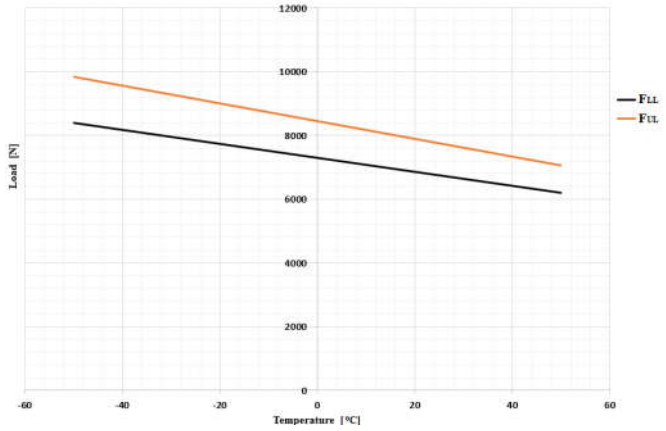

Figure 21 Influence of the temperature on the limit and ultimate load capacity of the joint, experimental results

CONCLUSIONS

In this paper, the thermal effects on the stiffness, damage initiation and progressive failure for single-lap, multiple-bolts, hybrid metal-composite joints are investigated using both experimental technique and simulations with finite element method (FEA). Regarding the first ply failure (FPF) and strength evaluations, a progressive damage analysis (PDA) including lamina nonlinear shear behavior, Hashin's failure criteria and strain-based continuous degradation rules was proposed. A 3D FEM model, which incorporates geometrical and contact full nonlinearities was developed in Patran commercial software as preprocessor and Nastran as explicit iterative solver. The PDA material model was implemented using a user-defined subroutine namely USER_MAT, using FOTRAN programming language.

The simulation results were in good agreement with the experiments in terms of load-displacement behavior, surface strains, joint stiffness, FPF and ultimate loads, as can be seen from (Figs. 12, 13 and 14), which denoted that the 3D FEM model including full nonlinearities and explicit solver are quite accurate and can predict the metal-composite joint's structural behavior on both linear and nonlinear elastic ranges, including the failure modes as bearing and shear-out.

Regarding the thermal effects on the joint stiffness it can be seen from Table 6 that, temperature decreases the stiffness of the joint in the axial direction. The loading joint behavior released some interesting features at the beginning stage due to friction between the plates. This friction stage is composed from two parts: static and dynamic friction as can been seen from the load-displacement curves in Figs. 13 and 14. From these graphs it can be detected the friction load and, knowing the clamping force from torque level, therefore the friction coefficient between the plates can be calculated for the two temperatures study. Regarding the influence of temperature on the ultimate load of the joint, it has been observed that the load is decreasing while temperature is increasing, so as a global conclusion of the study, the temperature has reduced both the stiffness and strength of the joint.

References

Xiao Y, Ishikawa T, (2005). Bearing strength and failure behavior of bolted composite joints (part II: modeling and simulation). *Composites Science and Technology*, 65: 1032–1043.

Chaboche J (1988). Continuum damage mechanics: part I – General concepts; part II - damage growth, crack initiation and crack Growth. *Journal of Applied Mechanics*, 55: 59–72.

Chang F, Chang K, (1987). Post-failure analysis of bolted composite joints in tension or shear-out mode failure. *Journal of Composite Materials*, 21: 809–842.

Lessard L, Shokrieh M, (1995). Two-dimensional modeling of composite pinned-joint failure. *Journal of Composite Materials*,29: 671–768.

Hung C, Chang F, (1996). Bearing failure of bolted composite joints. Part II: model and verification. *Journal of Composite Materials*,30: 359-400.

Kim S, Hwang J, Kim J, (1998). Progressive failure analysis of pin-loaded laminated composites using penalty finite element method. *AIAA Journal*, 36(1): 75–80.

Camanho P, Matthews F,(1999). A progressive damage model for mechanically fastened joints in composite laminates. *Journal of Composite Materials*, 33: 2248–80.

Okutan B, (2002). The effects of geometric parameters on the failure strength for pin-loaded multi-directional fiber-glass reinforced epoxy laminate. Compos. B. Eng.33(8):567–8.

Tserpes K, Labeas G, Papanikos P, Kermanidis T, (2002). Strength prediction of bolted joints in graphite/epoxy composite laminates. *Compos. B. Eng*. 33(7): 521–9.

Olmedo Á, Santiuste C, (2012). On the prediction of bolted single-lap composite joints. *Composite Structures*, 94(6):2110–7.

Kapidz˘ic´ Z, Nilsson L, Ansell H, (2014). Finite element modeling of mechanically fastened composite-aluminum joints in aircraft structures. *Composite Structures*,109(6): 198–210.

Zerbst A, Kuhlmann G, Steenbock C, (2010). Progressive damage analysis of composite bolted joints with liquid shim layers using constant and continuous degradation models.*Composite Structures* 92(2): 189–200.

Kolks G, Tserpes K, (2014). Efficient progressive damage modeling of hybrid composite/titanium bolted joints. Composites A,56(1): 51-63.

Egan B, McCarthy M, Frizzell R, Gray P, McCarthy C, (2014). Modelling bearing failure in countersunk composite joints under quasi-static loading using 3D explicit finite element analysis. *Composite Structures*, 108: 963–977.

Olmedo A, Santiuste C, Barbero E, (2014). An analytical model for the secondary bending prediction in single-lap composite bolted-joints. *Composite Structures*,111: 354–361.

da Costa Mattos H, Reis J, Paim L, da Silva M, Amorim F, Perrut V, (2014). Analysis of a glass fibre reinforced polyurethane composite repair system for corroded pipelines at elevated temperatures. *Composite Structures*, 114:117-23.

Reis J, Coelho J, Monteiro A, da Costa Mattos H, (2012). Tensile behavior of glass/epoxy laminates at varying strain rates and temperatures. Composites Part B, 43:2041–6.

Reis J, Coelho J, da Costa Mattos H, (2013). A continuum damage model for glass/epoxy laminates in tension. Composites Part B;52:114–9.

Reis J, Amorim F, da Silva A, da Costa Mattos H, (2015). Influence of temperature on the behavior of DGEBA (bisphenol A diglycidyl ether) epoxy adhesive. *International Journal of Adhesion and Adhesives*;58:88–92.

Jiang Z, Wan S, Wu Z, (2016). Calculation of energy release rate for adhesive composite/metal joints under mode-I loading considering effect of the non-uniformity. Composites Part B;95:374–85.

Heshmati M, Haghani R, Al-Emrani M, (2017). Durability of bonded FRP-to-steel joints: effects of moisture, de-icing salt solution, temperature and FRP type. Composites Part B;119:153–67.

Kleffel T, Drummer D, (2017). Investigating the suitability of roughness parameters to assess the bond strength of polymer-metal hybrid structures with mechanical adhesion. Composites Part B;117:20–5.

Agarwal A, Foster S, Hamed E, (2015). Wet thermo-mechanical behavior of steel–CFRP joints – an experimental study. Composites Part B Eng;83:284–96.

Agarwal A, Foster S, Hamed E, Vrcelj Z. Testing of steel-CFRP adhesive joints under freeze-thaw cycling. From mater. To struct. Adv. Through innov. - proc. 22nd australas. Conf. Mech. Struct. Mater. ACMSM 2012; 2013. pp. 801–6.

Heshmati M, Haghani R, Al-Emrani M, (2016). Effects of moisture on the long-term performance of adhesively bonded FRP/steel joints used in bridges. Composites Part B Eng;92:1–16.

ASTM D 5961. Standard test method for bearing response of polymer matrix composite laminates (2007).

Maajid Ch, Chun H. W, Rodney S, Thomson B, Adrian C,(2012). Experimental investigation of damage progression and strength of countersunk composite joints, Composite Structures 94 865–873.

ASTM D 3039. Standard Test Method for Tensile Properties of Polymer Matrix Composite Materials (2002).

ASTM D 3410, Standard Test Method for Compressive Properties of Polymer Matrix Composite Materials, ASTM International, (2007).

ASTM D 5379, Standard Test Method for Shear Propeties of Composite Materials by the V-Notched Beam Method, ASTM International, (2008).

Torayca T300 Technical Data Sheet No. CFA-001, Toray Carbon Fibers America Inc, www.torayusa.com

Derakane Momentum 411-350 Epoxy Venyl Ester Resin, Technical Data Sheet No. 1701 V3 F2, Ashland Inc, www.ashland.com

ECSS-E-HB-32-20 Part 2A. Structural materials handbook - Part 2: Design calculation methods and general design aspects (2011).

MMPDS-05. Metallic Materials Properties development and Standardization (2010).

McCarthy M, McCarthy C, Lawlor V, Stanley W, (2005). Three-dimensional finite element analysis of single-bolt, single-lap composite bolted joints: part I-model development and validation. Composite Structures, 71:140–158.

Schon J, (2004). Coefficient of friction for aluminum in contact with a carbon fiber epoxy composite. *Tribology International*,37(5): 395-404.

Hahn H, Tsai S, (1973). Nonlinear elastic behavior of unidirectional composite laminates. *Journal of Composite Materials,* 7(1): 102–18.

Ao D, Yuqing L, Haohui X, Yize Z, (2016). Progressive damage analysis of PFRP double-lap bolted joints using explicit finite element method. Composite Structures, 152: 860–869.

Hashin Z, (1980). Failure criteria for unidirectional fiber composites. *Journal of Applied Mechanics*,47: 329-34.

Zhou Y, Yazdani-Nezhad H, Mccarthy M, (2014). A study of intra-laminar damage in double-lap, multi-bolt, composite joints with variable clearance using continuum damage mechanics. Composite Structures,116 (9):441-52.

O'Higgins R. An experimental and numerical study of damage initiation and growth in high strength glass and carbon fibre-reinforced composite materials [PhD]. University of Limerick, College of Engineering,(2007).

Lamb H,(1917). On Waves in an Elastic Plate, Proc. of the Royal Society, Mathematical, Physical and Engineering Sciences,93: 114-128.

Giurgiutiu V, Bao J, (2002). Embedded Ultrasonic Structural Radar with Piezoelectric Wafer Active Sensors for the NDE of Thin-Wall Structures, Proc. ASME International Mechanical Engineering Congress.

Giurgiutiu V, Lamb wave generation with piezoelectric wafer active sensors for structural health monitoring, San Diego: SPIE, (2003).

http://www.steminc.com/piezo/PZ_property.asp.

How to cite this article:

Calin-Dumitru COMAN. 2018, Thermal Effects on the Failure Mechanisms of Hybrid Metal-Composite Multi-Bolts Joints. *Int J Recent Sci Res.* 9(8), pp. 28407-28416. DOI: http://dx.doi.org/10.24327/ijrsr.2018.0908.2455

****